Energy Storage Materials 14 (2018) 246–252

Contents lists available at ScienceDirect

Energy Storage Materials

journal homepage: www.elsevier.com/locate/ensm

High energy density hybrid lithium-ion capacitor enabled by Co_3ZnC@N-doped carbon nanopolyhedra anode and microporous carbon cathode

Guoyin Zhu[a,1], Tao Chen[a,1], Lei Wang[a], Lianbo Ma[a], Yi Hu[a], Renpeng Chen[a], Yanrong Wang[a], Caixing Wang[a], Wen Yan[a], Zuoxiu Tie[a], Jie Liu[a,b], Zhong Jin[a,*]

[a] Key Laboratory of Mesoscopic Chemistry of MOE and Collaborative Innovation Center of Chemistry for Life Sciences, School of Chemistry and Chemical Engineering, Nanjing University, Nanjing, Jiangsu 210023, China
[b] Department of Chemistry, Duke University, Durham, NC, 27708, USA

ARTICLE INFO

Keywords:
Hybrid lithium-ion capacitors
Co_3ZnC@NC anodes
Microporous carbon cathodes
High energy densities
High power densities

ABSTRACT

Hybrid lithium-ion capacitors (HLICs) have drawn great attention as promising energy devices, because they can integrate the high energy density of lithium ion batteries and the high power density of supercapacitors, and their low cost and long cycling-life are well suited to large-scale energy storage. However, the development of HLICs is usually limited by the kinetics mismatch between the battery-type anode and capacitor-type cathode. In this study, hierarchical Co_3ZnC nanoparticle encapsulated mesoporous nitrogen-doped carbon nanopolyhedra (Co_3ZnC@NC) synthesized by one-step pyrolysis of bimetallic-organic-frameworks are used as anode material for HLICs, exhibit high lithium storage capacity and excellent rate performance. Moreover, heteroatom-doped microporous carbon (MPC) derived from nature-abundant biomass (pine needles) are employed as cathode material, demonstrating good rate capability and long cycle stability. As a result, the as-prepared Co_3ZnC@NC||MPC HLICs deliver high energy densities (up to 141.4 Wh kg^{-1}), high power densities (up to 10.3 kW kg^{-1}) and long cycle life within the wide operating voltage range (1.0–4.5 V). These encouraging results of the HLICs bridge the gap between supercapacitors and batteries, and show great potential in next-generation energy storage devices.

1. Introduction

With the ever-increasing demands for portable electronic devices, electric vehicles and large-scale grid storage, advanced energy-storage devices with high specific energy, large power and long cycle life are highly desired [1–3]. In particular, supercapacitors (SCs) and lithium ion batteries (LIBs) are attracting enormous attention due to the great promise as high-performance electrochemical power sources [4–6]. SCs hold great promise because of the fast charge delivery, high power density (~10 kW kg^{-1}) and long cycle life; however, the double-layer charge storage mechanism of SCs results in low energy density (usually ≤10 Wh kg^{-1}) [7,8]. Conversely, LIBs can provide high energy density (100–200 Wh kg^{-1}), but the sluggish intercalation/extraction of Li ions leads to low power density (less than 0.5 kW kg^{-1}), large volume variation and poor cycling stability [9,10]. Therefore, the current status of energy storage using LIBs or SCs is unable to fully satisfy the demands in terms of both energy and power for application in electric vehicles. Thus, it is strongly appealing to develop novel energy-storage systems that can compromise the merits of SCs and LIBs.

Hybrid lithium-ion capacitors (HLICs) have been regarded as a promising solution to bridge the gap between LIBs and SCs. The HLICs are composed of a Li-ion intercalating type anode to provide high energy density and an electric-double-layer-forming cathode to ensure high power density [11–13]. With this configuration, the HLICs can store charge by utilizing a reversible lithium insertion/extraction reaction in the anode, and a simultaneously reversible adsorption/desorption reaction of anions on the surface of the cathode. Therefore, The HILCs exhibit remarkably enhanced energy densities compared to conventional SCs. However, because the anode kinetics based on the lithiation/delithiation is slower than that of the ion adsorption/desorption kinetics on the cathode material, the power density and cycle stability of HLICs are seriously restricted [14–16]. Therefore, the rational design and fabrication of suitable anode materials with fast kinetics process are imperative for the development of high performance HLICs.

* Corresponding author.
E-mail address: zhongjin@nju.edu.cn (Z. Jin).
[1] These authors contributed equally to this work.

https://doi.org/10.1016/j.ensm.2018.04.009
Received 8 February 2018; Received in revised form 8 April 2018; Accepted 8 April 2018
Available online 09 April 2018

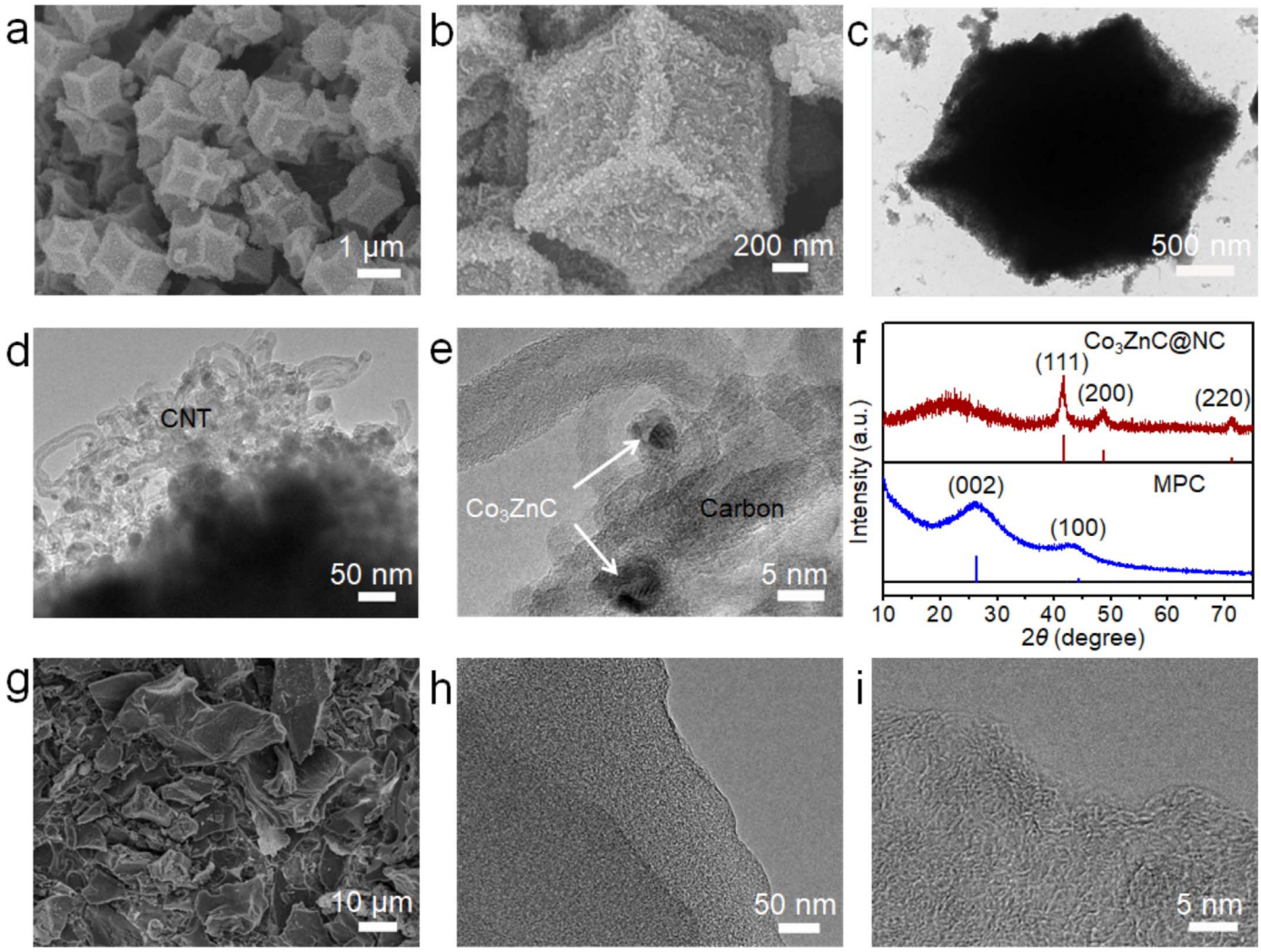

Fig. 1. (a, b) SEM and (c-e) TEM images of Co_3ZnC@NC. (f) XRD patterns of Co_3ZnC@NC and MPC. (g) SEM and (h, i) TEM images of MPC.

To alleviate the kinetics imbalance between the anode and cathode sides of HLICs, an effective strategy is developing pseudocapacitive anode materials with rapid and reversible redox kinetics, which is not diffusion-limited but surface-limited [17,18]. Up to now, some anode materials with obvious pseudocapacitive properties, such as Nb_2O_5/graphene [19,20], TiO_2@graphene [21,22], and MoO_3/graphene nanosheets [23], have been proposed for improving the anode kinetics. However, the poor electrical conductivity and the inappropriate voltage plateau of metal oxides may greatly reduce the operating voltage range and the energy density of HLICs [24–26]. Intriguingly, transition-metal carbides (TMCs) appear to be promising candidates for lithium storage due to excellent chemical stability, fast kinetics and good electrical conductivity [27]. For instances, layered TMCs (such as Ti_2C, Ti_3C_2, V_2C and Mo_2C) [28–31], known as "MXenes", have demonstrated pseudocapacitive Li-ion storage behavior and fast ion accessibility to redox sites. Recently, Liu et al. has found that Co_3ZnC nanoparticle encapsulated mesoporous carbon nanostructures derived from Prussian blue analogues can be applied as high capacity, good rate capability and ultralong-life anode materials in LIBs [32]. We expect that anode materials based on TMCs also have great potential to be used in HLICs.

On the other hand, unlike the extensive investigations into anode materials, very few reports about the exploration of new cathode materials for HLICs were reported. Commercially-available activated carbon (AC) was often used as cathode material in HLICs owing to the large surface area. However, the overall capacity of HLICs (C_{HLIC}) were seriously limited by the low specific capacity of AC cathode (30–35 mAh g^{-1}) [25], according to the equation ($1/CH_{LIC} = 1/C_{cathode} + 1/C_{anode}$) [33,34]. Hence, the design of novel cathode materials with good conductivity, large surface area and suitable pore distribution are important for HLICs.

Based on the above considerations, here we report the remarkable performance improvement of HLICs by utilizing ternary metal carbide Co_3ZnC nanoparticle encapsulated nitrogen-doped mesoporous carbon nanopolyhedra (Co_3ZnC@NC) as anode material and heteroatom-doped microporous carbon (MPC) as cathode material. The Co_3ZnC@NC was synthesized by direct pyrolysis of bimetallic ZIFs with ordered morphology [35]. With the advantages of the hierarchical structure and pseudocapacitive properties, the Co_3ZnC@NC electrodes exhibit high lithium storage capacity, excellent rate performance and long cycling stability. Moreover, nitrogen- and oxygen-doped MPC derived from nature-abundant pine needles were explored as cathode material [36], which can facile prepared with low cost for large-scale production. The large specific surface area and high oxygen content (~7.8 at%) of MPC are in favor of increasing the specific capacity. By employing these electrode materials, the as-prepared Co_3ZnC@NC||MPC HLICs exhibit a wide operating voltage range (1.0–4.5 V), an ultrahigh energy density (141.4 Wh kg^{-1}) and a large power density (10.3 kW kg^{-1}), which are competitive among the existing HLICs (Table S1) [15,20–22,25,37–47].

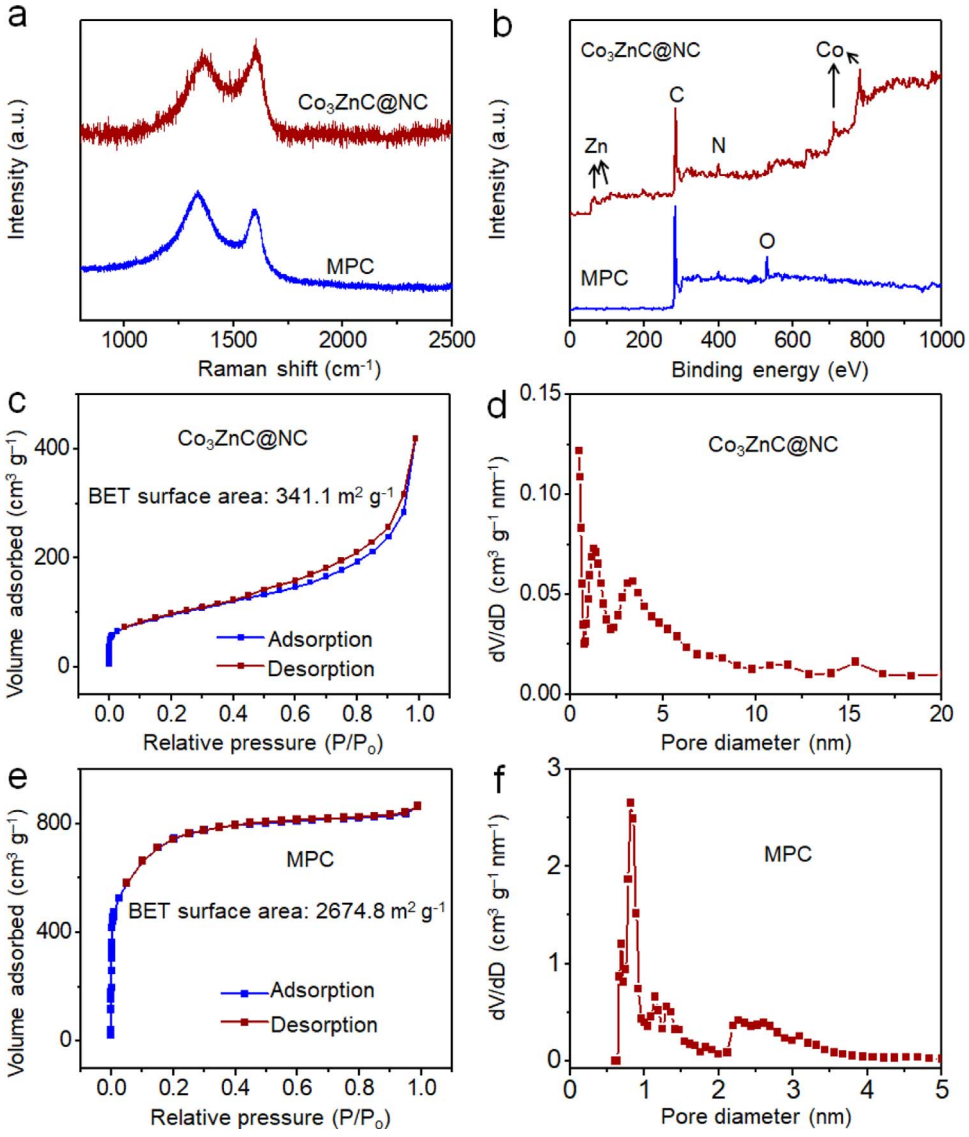

Fig. 2. (a) Raman spectra and (b) XPS spectra of Co_3ZnC@NC and MPC, respectively. Nitrogen adsorption-desorption isotherms and pore size distribution curves of (c, d) Co_3ZnC@NC and (e, f) MPC, respectively.

2. Result and discussion

The synthesis process of Co_3ZnC@NC was schematically illustrated in Scheme S1 and detailed in the Experimental Section. Briefly, bimetallic ZnCo-zeolite imidazolate framework (ZnCo-ZIF) precursor with dodecahedron morphology was prepared by a co-precipitation method, and then heated under Ar/H_2 and Ar atmosphere to convert the ZnCo-ZIF nanopolyhedra into Co_3ZnC@NC [35]. The morphology and structure of Co_3ZnC@NC were investigated by scanning electron microscopy (SEM) and transmission electron microscopy (TEM) (Fig. 1a-e). After the thermal treatment, the resultant Co_3ZnC@NC polyhedra exhibit similar polyhedral morphology and size of ZnCo-ZIF precursor, but with highly-rough surface and tangled carbon nanotubes grown on the outer surface (Fig. 1a, b). The concave morphology of Co_3ZnC@NC should be resulted from the carbonation process. Notably, the carbon nanotubes were in-situ grown on the surface of Co_3ZnC@NC, because the Co species in ZnCo-ZIF served as the nanocatalysts and the organic species served as the carbon source for the growth of carbon nanotubes under Ar/H_2 atmosphere [48]. As shown in Fig. 1c-e, the Co_3ZnC@NC show polyhedron structure, in which the Co_3ZnC nanoparticles are homogenously encapsulated in the matrix of N-doped porous carbon. Moreover, it was revealed that numerous carbon nanotubes were grown on the concave surface of Co_3ZnC@NC (Fig. 1d,e), in accordance with SEM characterizations. The interconnected network of carbon nanotubes and nanopolyhedra allow fast ion/electron transport and facilitate electrochemical diffusion of lithium ions. The crystal structure of Co_3ZnC@NC was characterized by powder X-ray diffraction (XRD). As shown in Fig. 1f, the XRD peaks of Co_3ZnC@NC are located at 41.4°, 48.8°, and 71.4°, in agreement with cubic Co_3ZnC (JCPDS No. 29-0524) [27].

The detailed synthesis process of MPC is described in the Experimental Section [36]. As shown in the SEM and TEM images (Fig. 1g-i), the MPC is composed of microscale carbon granules with uniformly distributed micropores, which can provide favorable pathways for ion diffusion. The MPC showed broad XRD peaks originated from the (002) and (100) crystal planes of partially-graphitized porous carbon, and no other impurity peaks were detected.

Raman spectra were measured to further reveal the microstructures of Co_3ZnC@NC and MPC (Fig. 2a). Two broad peaks at around 1350 cm^{-1} and 1580 cm^{-1} were observed, corresponding to the D band (defects) and G band (C-C stretching of sp^2 carbon), respectively [22]. The compositions of Co_3ZnC@NC were determined by X-ray photoelectron spectroscopy (XPS, Fig. 2b), reveals the co-existence of Zn, Co, C, and N elements. As shown in Figure S1a, the high-resolution XPS

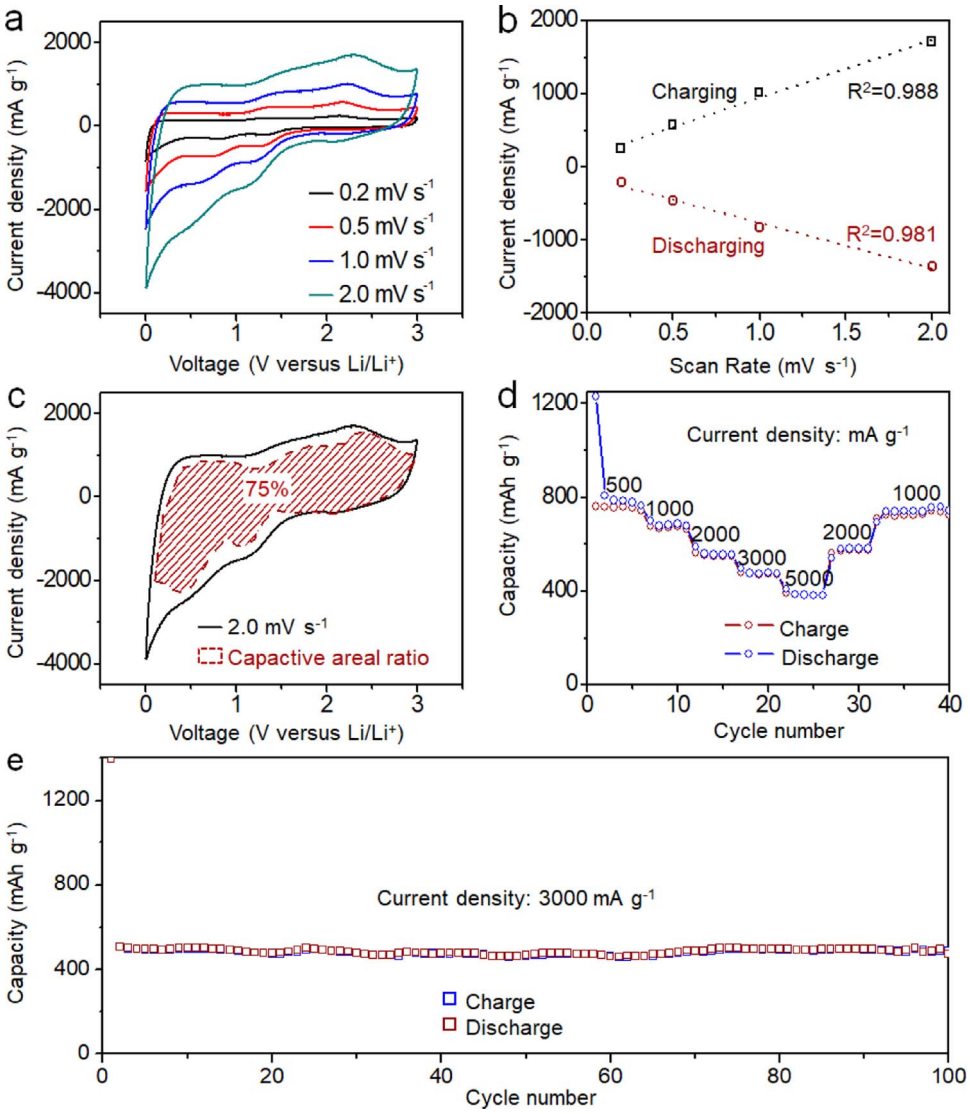

Fig. 3. Electrochemical properties of Co_3ZnC@NC electrode. (a) CV curves at various scan rates. (b) Correlations of charging/discharging peak current densities and scan rates. (c) CV response at a scan rate of 2.0 mV s^{-1}. The part of capacitive contribution is marked by the red shaded region. (d) Rate performance at different current densities. (e) Long-term cycling stability at a large current density of 3000 mA g^{-1}.

spectrum at Co 2p region of Co_3ZnC@NC exhibited two energy bands of 781.1 eV (Co $2p_{3/2}$) and 796.2 eV (Co $2p_{1/2}$), respectively. The energy band of N 1 s (Figure S1b) was mainly originated from pyridinic-N (398.5 eV), pyrrolic-N (399.5 eV) and graphitic-N (401.2 eV), respectively. The energy-dispersive X-ray spectroscopy (EDX) analysis of Co_3ZnC@NC (Figure S2) shows the presence of Zn, Co, C, and N, in line with the XPS results. The content of N in Co_3ZnC@NC was estimated to be 15.9 at%, which can provide abundant active sites for lithium storage. Thermogravimetric analysis (TGA) was conducted to evaluate the contents of Co_3ZnC and NC in the composite. As shown in the Figure S3, the weight loss was 6.1% when the temperature increased from room temperature to 200 °C under air atmosphere, owing to the degassing and removal of water. The weight loos reached 43.7% when the temperature increased to 600 °C. Based on the weight loss, the weight contents of Co_3ZnC and NC were estimated to be 60.0% and 40.0%, respectively.

The XPS analysis of MPC indicated the existence of C, N and O species, and the N and O contents were determined to be 1.2 and 7.8 at %. The high-resolution XPS spectrum at C 1s region of MPC (Figure S1c) could be identified into five peaks at around 284.6, 285.6, 286.2, 287.2 and 289.9 eV, corresponding to C=C, C-N, C-O, C=O and O-C=O, respectively. The O 1s energy band of MPC (Figure S1d) can be fitted into four main peaks: C=O (531.5 eV), C-O (532.5 eV), C-O-C (532.7), and −OH (533.5 eV). These functional groups could enhance the wettability and capacity of MPC [49,50]. The nitrogen adsorption-desorption isotherms and pore size distribution curves of Co_3ZnC@NC and MPC are shown in Fig. 2c-f. The Co_3ZnC@NC exhibited a Brunauer-Emmett-Teller (BET) surface area of 341.1 m^2 g^{-1} with the pore size distribution centered around 3.5 nm (Fig. 2c-d). The hierarchical porosity of Co_3ZnC@NC could be beneficial to smooth ion transfer. The nitrogen adsorption-desorption isotherms of MPC (Fig. 2e) exhibits a typical type I behavior, implying the presence of microporous structure. The BET surface area of MPC is measured to be 2674.8 m^2 g^{-1}, which contributes to the capacitance of HLICs. Through the Quenched Solid Density Functional Theory (QSDFT) method, the pore size distribution of MPC was determined (Fig. 2f), revealing abundant micropores (0.8–2 nm) and mesopores (2–4 nm). The size of mesopores (2–4 nm) is larger than the size of the solvated ions, thus very beneficial to the electrolyte immersion and retention. Moreover, the ions in electrolyte can smoothly move along the mesopores and get easy access to the micropores, providing favorable pathways for ions transport [1,50]. Meanwhile, the micropores with the diameter larger than 0.8 nm are accessible to PF_6^- anions, which can further enhance the charge storage [51–53]. Hence, the multi-scale hierarchical porous

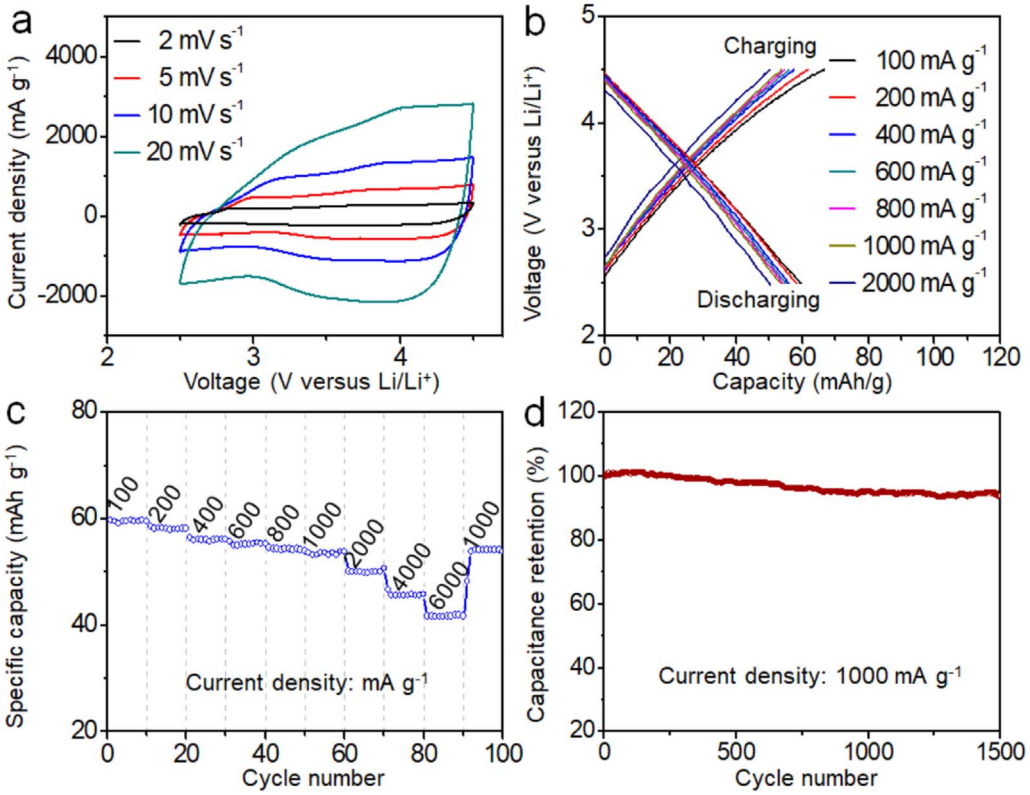

Fig. 4. Electrochemical properties of MPC electrode. (a) CV curves at various scan rates. (b) Galvanostatic charging/discharging curves. (c) Rate performance at different current densities. (d) Cycling performance at a high current density of 1000 mA g^{-1}.

structure of the MPC is very helpful to improve the energy density and the power capability HLICs.

The inherent electrochemical performance of Co_3ZnC@NC electrode was firstly investigated by half-cell tests. Cyclic voltammetry (CV) measurements were carried out at different scan rates ranged from 0.2 to 2.0 mV s^{-1} (Fig. 3a). The broad cathodic and anodic peaks suggest the Li^+ insertion/extraction reactions of Co_3ZnC@NC. Generally, the Li ions intercalation kinetics can be analyzed by the dependence of cathodic and anodic peak currents i on the scan rate v:

$$i = av^b \quad (1)$$

where a and b are appropriate parameters. If b = 0.5, it indicates a semi-infinite diffusion process controlled by Li^+ intercalation; while b = 1 suggests a capacitive behavior caused by surface redox reactions [17,54]. Therefore, for the active materials with pseudocapacitive behavior, the peak current i should vary linearly with the scan rate (v). As shown in Fig. 3b, the Co_3ZnC@NC electrode exhibited a good linear correlation between the peak current and the sweep rate, with R^2 = 0.988 and 0.981 for the charging and discharging curves, respectively. This implies that the electrochemical kinetics of Co_3ZnC@NC electrode is mainly contributed from surface-controlled pseudocapacitive behavior [25,55]. To distinguish the capacitive contribution to the current response of CV curves, Eq. (1) is rewritten as

$$i = k_1v + k_2v^{1/2} \quad (2)$$

where k_1 and k_2 are adjustable values [56,57]. The current at a fixed potential can be a combination of two separate mechanisms, capacitive behavior (k_1v) and diffusion-controlled process ($k_2v^{1/2}$). The k_1 and k_2 values at the different potentials can be obtained by plotting the curves of $iv^{1/2}$ *vs.* $v^{1/2}$. By calculating the capacitive contribution (red shaded region) with the total area (solid line) in Fig. 3c, the capacitive contribution is estimated to be 75%. This result indicates that the Li^+ storage behavior in the Co_3ZnC@NC electrode can be predominately attributed to a pseudocapacitive mechanism [25,27].

The obvious redox peaks in the capacitive region further demonstrate the pseudocapacitive property of Co_3ZnC@NC. The galvanostatic charging-discharging curves of Co_3ZnC@NC electrode at 500 mA g^{-1} (Figure S4) exhibit smooth shapes since the second cycle, which also indicates the pseudocapacitive behavior. The capacity of Co_3ZnC@NC electrode decreased slowly as the current densities increased from 500 to 5000 mA g^{-1} (Fig. 3d), and well recovered when the current density reduced back to 1000 mA g^{-1}, indicating the excellent rate capability of Co_3ZnC@NC. Additionally, the Co_3ZnC@NC electrode shows good cycle stability with an overall capacity decay of only ~5% after 100 charging/discharging cycles at the large current density of 3000 mA g^{-1} (Fig. 3e). To understand the remarkable kinetic properties of Co_3ZnC@NC electrode, electrochemical impedance spectra (EIS) before and after long-term cycling were measured. As shown in Figure S5, the charge transfer resistance after 100 cycles is much smaller than those before cycling, which is attributed to the activation process of porous carbon matrix with the electrolyte.

The remarkable electrochemical performances of Co_3ZnC@NC electrode can be ascribed to the well-organized 3D framework constructed by Co_3ZnC nanoparticles and porous carbon matrix. First, the porous carbon matrix can provide smooth pathways for electron/ion transport. Second, the ultrafine Co_3ZnC nanoparticles are conducive to fast Li^+ insertion/extraction. Third, the numerous carbon nanotubes grown on the surface of nanopolyhedra can improve the overall electronic conductivity of electrode.

The electrochemical performances of MPC electrode were also evaluated by CV and galvanostatic charging-discharging processes in a half-cell system (Fig. 4). The potential range was set between 2.5 and 4.5 V (vs Li/Li^+) to provide a large potential window for HLICs. The CV curves of MPC electrode at various scan rates from 2.0 to 20 mV s^{-1} (Fig. 4a) show quasi-rectangular shapes, suggesting the dominant electric double layer capacitance (EDLC) and subordinate pseudocapacitance. The minor redox reactions were originated from the functional groups on the surface of MPC. The galvanostatic charging/

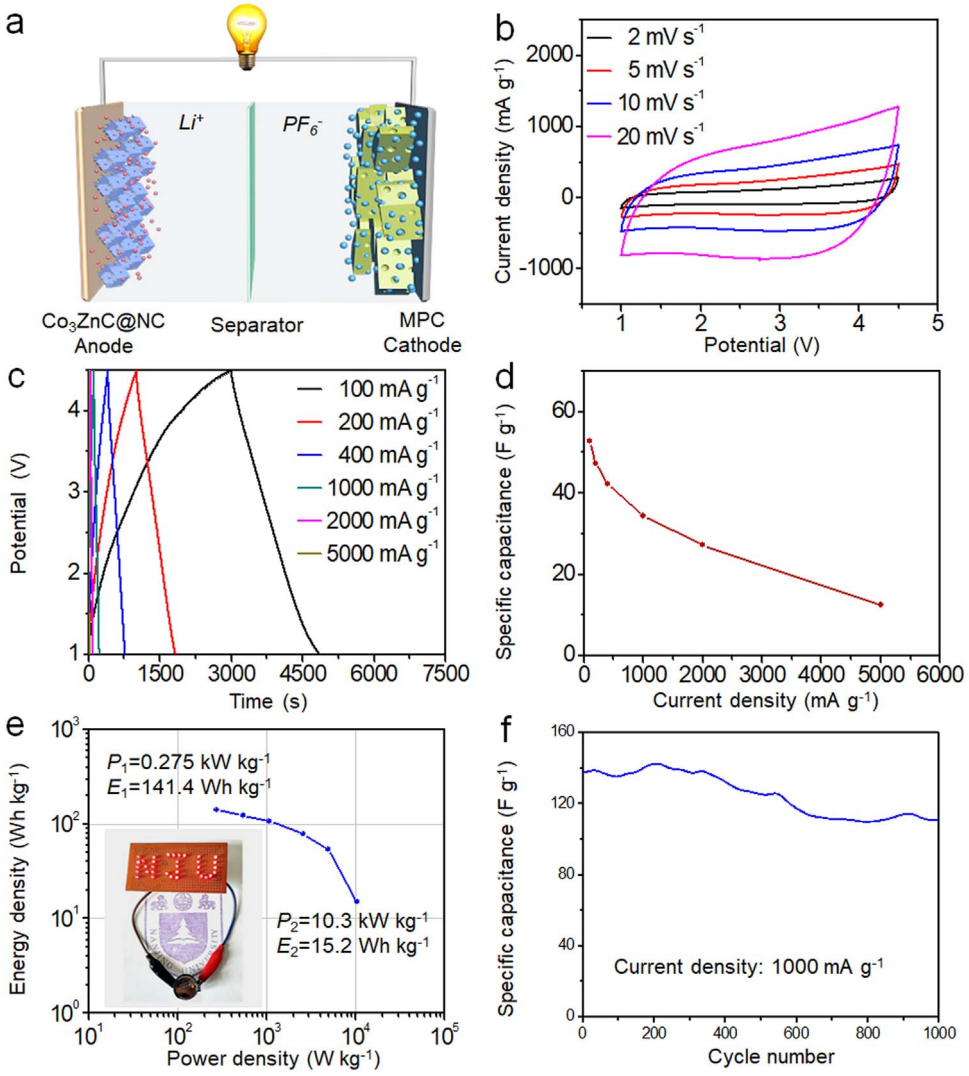

Fig. 5. Electrochemical performances of HLICs with the Co_3ZnC@NC||MPC configuration. (a) Schematic illustration of HLICs with Co_3ZnC@NC as anode material and MPC as cathode material. (b) CV curves of HLICs between 1.0 and 4.5 V at various scan rates. (c) Charging-discharging curves of HLICs at different current densities. (d) Rate performance of HLICs at different current densities. (e) Ragone plots of HLICs. The inset is an optical photograph showing a pattern of "NJU" consisting of 34 red LEDs simultaneously lighted by a HLIC. (f) Cycling performance of HLICs at a current density of 1000 mA g^{-1}.

discharging curves of MPC electrode (Fig. 4b) show almost linear relations, further indicating the predominated EDLC behavior. Owing to the high surface area and abundant micropores, the MPC electrode exhibited a relatively high specific capacity of 59.6 mAh g^{-1} at 100 mA g^{-1} (Fig. 4c), much higher than that of commercially-available activated carbon (AC, 35 mAh g^{-1}) [23]. The specific capacity of MPC electrode reached 41.7 mAh g^{-1} at a high current density of 6000 mA g^{-1}, exhibiting an excellent rate capability, which could be ascribed to the low charge transfer resistance and appropriate surface functional groups that can facilitate ion transport [49,51]. After 1500 cycles at 1000 mA g^{-1}, the MPC electrode still retained ~93% of the initial capacity (Fig. 4d), indicating a superior cycling stability. This result is also supported by EIS analyses, as shown in Figure S6. Obviously, the semicircle in the ESI curve of MPC electrode after 1500 cycles is smaller than that of the fresh electrode, implying a decreased charge transfer impedance.

On the basis of the excellent performances of Co_3ZnC@NC and MPC in the half-cell tests, we assembled full-cell HLICs with Co_3ZnC@NC||MPC configuration. As shown in Fig. 5a, during the charging processes, Li^+ ions from the electrolyte can be quickly intercalated into the Co_3ZnC@NC anode, while PF_6^- ions rapidly adsorb onto/into the MPC cathode. The CV curves of HLICs at different scan rates show quasi-rectangular shapes (Fig. 5b), suggesting that the kinetics of anode and cathode is well matched and balanced [23]. Moreover, the galvanostatic charging-discharging profiles exhibit quasi-symmetric triangular shapes (Fig. 5c) further confirming that the pseudo-capacitance of Co_3ZnC@NC anode and the EDLC of MPC cathode are well combined in the device. At the current density of 5000 mA/g, the charging-discharging cycles can be finished within 20 s, indicating a superior rate performance. The cell-discharge capacitance (C_{cell}) and the specific capacitance (C_s) of HLICs were calculated with the following equations [58,59]:

$$C_{cell} = (it/\Delta V) \quad (3)$$

$$C_s = (C_{cell}/m) \quad (4)$$

where i is the applied current, t is the discharging time, ΔV is the voltage range and m is the total mass of anode and cathode. The calculated C_s values at different current densities are shown in Fig. 5d, which demonstrates a superb capacitance of ~52.8 F g^{-1} at a current density of 100 mA g^{-1}.

Fig. 5e presents the Ragone plots (energy density *vs.* power density) of the Co_3ZnC@NC||MPC HLICs. The maximum energy density of the HLICs is as high as 141.4 Wh kg^{-1} at a low power density of 0.275 kW kg^{-1} (100 mA g^{-1}). Even at a high power density of

10.3 kW kg^{-1}, the HLICs still can deliver an energy density of 15.2 Wh kg^{-1}, suggesting the favorable properties from the synergetic advantages of LIBs and SCs. The remarkable energy density and power capability of the Co_3ZnC@NC||MPC HLICs are competitive among other existing HLICs in previous reports (Table S1) [15,20–22,25,37–47]. As a demonstration, a pattern of "NJU" logo consisting of 34 red LEDs was simultaneously lighted by a coin-cell of Co_3ZnC@NC||MPC HLIC (inset of Fig. 5e). Long-term cycling tests were also performed to evaluate the cycling stability of the HLICs (Fig. 5f), presenting a high capacity retention of ~80% after 1000 cycles at the current density of 1000 mA g^{-1}, which is competitive among the existing HLICs [15,20–22,25,37–47].

3. Conclusion

The outstanding electrochemical performances of the Co_3ZnC@NC||MPC HLICs can be attributed to the following aspects: (1) The pseudocapacitive properties of Co_3ZnC@NC facilitates the rapid kinetics process, and the hierarchical porous framework of Co_3ZnC@NC with tangled carbon nanotubes can ensure interconnected conductive channels for electron/ion transport. (2) The high surface area, abundant micropores, and heteroatom doping of MPC are favorable for fast charge transfer and high specific capacity. (3) The well-matched Co_3ZnC@NC anode and MPC cathode can alleviate the kinetics imbalance in HLICs. As a result, the as-fabricated HLICs exhibited large working voltage window (1.0 V–4.5 V), high energy density (up to 141.4 Wh kg^{-1}) and power density (up to 10.3 kW kg^{-1}). We expect this work on HLICs could provide new inspiration to the design of next generation hybrid electrochemical energy-storage systems by integrating the superiorities of LIBs and SCs.

Acknowledgements

This work is supported by National Key R & D Program of China (2017YFA0208200, 2016YFB0700600, 2015CB659300), Projects of NSFC (21573108, 51761135104), Natural Science Foundation of Jiangsu Province (BK20150583, BK20170644), High-Level Entrepreneurial and Innovative Talents Program of Jiangsu Province, and the Fundamental Research Funds for the Central Universities (020514380107).

Appendix A. Supporting information

Supplementary data associated with this article can be found in the online version at doi:10.1016/j.ensm.2018.04.009.

References

[1] P. Simon, Y. Gogotsi, Nat. Mater. 7 (2008) 845–854.
[2] M. Armand, J.M. Tarascon, Nature 451 (2008) 652–657.
[3] J. Yan, Q. Wang, T. Wei, Z.J. Fan, Adv. Energy Mater. 4 (2014) 1300816.
[4] P. Poizot, S. Laruelle, S. Grugeon, L. Dupont, J.M. Tarasco, Nature 407 (2000) 496–499.
[5] P. Simon, Y. Gogotsi, B. Dunn, Science 343 (2014) 1210–1211.
[6] Y. Wang, R. Chen, T. Chen, H. Lv, G. Zhu, L. Ma, C. Wang, Z. Jin, J. Liu, Energy Storage Mater. 4 (2016) 103–129.
[7] X.Y. Shan, Y.Z. Wang, D.W. Wang, F. Li, H.M. Cheng, Adv. Energy Mater. 6 (2016) 1502064.
[8] J. Zhao, H. Lai, Z.Y. Lyu, Y.F. Jiang, K. Xie, X.Z. Wang, Q. Wu, L.J. Yang, Z. Jin, Y.W. Ma, J. Liu, Z. Hu, Adv. Mater. 27 (2015) 3541–3545.
[9] Z.S. Wu, W.C. Ren, L. Wen, L.B. Gao, J.P. Zhao, Z.P. Chen, G.M. Zhou, F. Li, H.M. Cheng, ACS Nano 4 (2010) 3187–3194.
[10] N.S. Choi, Z. Chen, S.A. Freunberger, X. Ji, Y.-K. Sun, K. Amine, G. Yushin, L.F. Nazar, J. Cho, P.G. Bruce, Angew. Chem. 51 (2012) 9994–10024.
[11] V. Aravindan, J. Gnanaraj, Y.S. Lee, S. Madhavi, Chem. Rev. 114 (2014) 11619–11635.
[12] J. Niu, R. Shao, M. Liu, J. Liang, Z. Zhang, M. Dou, Y. Huang, F. Wang, Energy Storage Mater. 12 (2018) 145–152.
[13] X. Wang, C. Yan, J. Yan, A. Sumboja, P.S. Lee, Nano Energy 11 (2015) 765–772.
[14] Y. Ma, H. Chang, M. Zhang, Y. Chen, Adv. Mater. 27 (2015) 5296–5308.
[15] R. Yi, S. Chen, J. Song, M.L. Gordin, A. Manivannan, D. Wang, Adv. Funct. Mater. 24 (2014) 7433–7439.
[16] (a) K. Leng, F. Zhang, L. Zhang, T.F. Zhang, Y.P. Wu, Y.H. Lu, Y. Huang, Y.S. Chen, Nano Res. 6 (2013) 581–592;
(b) G. Wang, C. Lu, X. Zhang, B. Wan, H. Liu, M. Xia, H. Gou, G. Xin, J. Lian, Y. Zhang, Nano Energy 36 (2017) 46–57.
[17] V. Augustyn, J. Come, M.A. Lowe, J.W. Kim, P.L. Taberna, S.H. Tolbert, H.D. Abruña, P. Simon, B. Dunn, Nat. Mater. 12 (2013) 518–522.
[18] Y. Wang, Z. Hong, M. Wei, Y. Xia, Adv. Funct. Mater. 22 (2012) 5185–5193.
[19] L.P. Wang, L.H. Yu, R. Satish, J.X. Zhu, Q.Y. Yan, M. Srinivasan, Z.C. Xu, RSC Adv. 4 (2014) 37389–37394.
[20] L.P. Kong, C.F. Zhang, J.T. Wang, W.M. Qiao, L.C. Ling, D.H. Long, ACS Nano 9 (2015) 11200–11208.
[21] H. Kim, M.Y. Cho, M.H. Kim, K.Y. Park, H. Gwon, Y. Lee, K.C. Roh, K. Kang, Adv. Energy Mater. 3 (2013) 1500–1506.
[22] F.X. Wang, C. Wang, Y.J. Zhao, Z.C. Liu, Z. Chang, L. j Fu, Y.S. Zhu, Y.P. Wu, D.Y. Zhao, Small 12 (2016) 6207–6213.
[23] W.W. Liu, J.D. Li, K. Feng, A. Sy, Y.S. Liu, L. Lim, G. Lui, R. Tjandra, L. Rasenthiram, G. Chiu, A.P. Yu, ACS Appl. Mater. Interfaces 8 (2016) 25941–25953.
[24] R. Wang, J. Lang, P. Zhang, Z. Lin, X. Yan, Adv. Funct. Mater. 25 (2015) 2270–2278.
[25] H. Wang, Y. Zhang, H.X. Ang, Y.Q. Zhang, H.T. Tan, Y.F. Zhang, Y.Y. Guo, J.B. Franklin, X.L. Wu, M. Srinivasan, Adv. Funct. Mater. 26 (2016) 3082–3093.
[26] G. Li, X. Wang, F.M. Hassan, M. Li, R. Batmaz, X. Xiao, A. Yu, ChemElectroChem 2 (2015) 1264–1269.
[27] Y. Xiao, P. Sun, M. Cao, ACS Nano 8 (2014) 7846–7857.
[28] M. Naguib, J. Come, B. Dyatkin, V. Presser, P.L. Taberna, P. Simon, M.W. Barsoum, Y. Gogotsi, Electrochem. Commun. 16 (2012) 61–64.
[29] S.J. Kim, M. Naguib, M.Q. Zhao, C.F. Zhang, H.T. Jung, M.W. Barsoum, Y. Gogotsi, Electrochim. Acta 163 (2015) 246–251.
[30] M. Naguib, J. Halim, J. Lu, K.M. Cook, L. Hultman, Y. Gogotsi, M.W. Barsoum, J. Am. Chem. Soc. 135 (2013) 15966–15969.
[31] J. Halim, S. Kota, M.R. Lukatskaya, M. Naguib, M.Q. Zhao, E.J. Moon, J. Pitock, J. Nanda, S.J. May, Y. Gogotsi, M.W. Barsoum, Adv. Funct. Mater. 26 (2016) 3118–3127.
[32] L.B. Ma, T. Chen, G.Y. Zhu, Y. Hu, H.L. Lu, R.P. Chen, J. Liang, Z.X. Tie, Z. Jin, J. Liu, J. Mater. Chem. A 4 (2016) 15041–15048.
[33] L.Y. Chen, Y. Hou, J.L. Kang, M.W. Chen, J. Mater. Chem. A 2 (2014) 8448–8455.
[34] H. Wang, C. Zhu, D. Chao, Q. Yan, H.J. Fan, Adv. Mater. 29 (2017) 1702093.
[35] T. Chen, B. Cheng, R. Chen, Y. Hu, H. Lv, G.Y. Zhu, Y. Wang, L. Ma, J. Liang, Z. Tie, Z. Jin, J. Liu, ACS Appl. Mater. Interfaces 8 (2016) 26834–26841.
[36] G.Y. Zhu, L. Ma, H. Lv, Y. Hu, T. Chen, R. Chen, J. Liang, X. Wang, Y. Wang, C.Y.Z. Tie, Z. Jin, J. Liu, Nanoscale 9 (2017) 1237–1243.
[37] H.P. Du, H. Yang, C.S. Huang, J.J. He, H.B. Liu, Y.L. Li, Nano Energy 22 (2016) 615–622.
[38] J.H. Lee, H.K. Kim, E. Baek, M. Pecht, S.H. Lee, Y.H. Lee, J. Power Sources 301 (2016) 348–354.
[39] L. Gao, D. Huang, Y. Shen, M. Wang, J. Mater. Chem. A 3 (2015) 23570–23576.
[40] R.V. Salvatierra, D. Zakhidov, J. Sha, N.D. Kim, S.K. Lee, A.R.O. Raji, N. Zhao, J.M. Tour, ACS Nano 11 (2017) 2724–2733.
[41] E. Lim, C. Jo, H. Kim, M.H. Kim, Y. Mun, J. Chun, Y. Ye, J. Hwang, K.S. Ha, K.C. Roh, K. Kang, S. Yoon, J. Lee, ACS Nano 9 (2015) 7497–7505.
[42] W. Siang, V. Lee, X. Huang, T.L. Tan, J.M. Xue, ACS Appl. Mater. Interfaces 10 (2018) 1690–1700.
[43] S. Jayaraman, S. Madhavi, V. Aravindan, J. Mater. Chem. A 6 (2018) 3242–3248.
[44] S.N. Liu, J. Zhou, Z.Y. Cai, G.Z. Fang, Y.S. Cai, A.Q. Pan, S.Q. Liang, J. Mater. Chem. A 4 (2016) 17838–17847.
[45] C.F. Liu, C.K. Zhang, H.Y. Fu, X.H. Nan, G.Z. Cao, Adv. Energy Mater. 7 (2017) 1601127.
[46] S. Dsoke, B. Fuchs, E. Gucciardi, M.W. Mehrens, J. Power Sources 282 (2015) 385.
[47] A. Chaturvedi, P. Hu, V. Aravindan, C. Kloc, S. Madhavi, J. Mater. Chem. A 5 (2017) 9177–9181.
[48] H. Li, Y. Su, W.W. Sun, Y. Wang, Adv. Funct. Mater. 26 (2016) 8345–8353.
[49] W.J. Qian, F.X. Sun, Y.H. Xu, L.H. Qiu, C.H. Liu, S.D. Wang, F. Yan, Energy Environ. Sci. 7 (2014) 379–386.
[50] Y. Wang, Y. Song, Y. Xia, Chem. Soc. Rev. 45 (2016) 5925–5950.
[51] B. Li, F. Dai, Q.F. Xiao, L. Yang, J.M. Shen, C.M. Zhang, M. Cai, Adv. Energy Mater. 6 (2016) 1600802.
[52] L. Eliad, G. Salitra, A. Soffer, D. Aurbach, J. Phys. Chem. B 105 (2001) 6880–6887.
[53] M. Endo, T. Maeda, T. Takeda, Y. Kim, K. Koshiba, H. Hara, M. Dresselhaus, J. Electrochem. Soc. 148 (2001) A910–A914.
[54] T. Brezesinski, J. Wang, J. Polleux, B. Dunn, S.H. Tolbert, J. Am. Chem. Soc. 131 (2009) 1802–1809.
[55] M. Yang, Y. Zhong, J.J. Ren, X.L. Zhou, J.P. Wei, Z. Zho, Adv. Energy Mater. 5 (2015) 1500550.
[56] T. Brezesinski, J. Wang, S.H. Tolbert, B. Dunn, Nat. Mater. 9 (2010) 146–151.
[57] X. Deng, Z. Wei, C. Cui, Q. Liu, C. Wang, J. Ma, J. Mater. Chem. A 6 (2018) 4013–4022.
[58] C.W. Liew, S. Rames, Materials 7 (2014) 4019–4033.
[59] J.H. Won, H.M. Jeong, J.K. Kang, Adv. Energy Mater. 7 (2017) 1601355.